JGR Oceans

RESEARCH ARTICLE
10.1029/2024JC021726

Key Points:

- Most of the sediment accommodation on the northern Gulf of Mexico margin resides in a small number of large depressions termed minibasins
- Scales of depressions follow heavy-tailed distributions, which suggest self-organization of bathymetry through depression merger
- The largest depressions along the margin are also the most topographically complex, housing nested depressions within depressions

Correspondence to:
K. M. Straub,
kmstraub@tulane.edu

Citation:
Reece, J. K., & Straub, K. M. (2025). Statistics of depressions covering the northern Gulf of Mexico salt-minibasin province: Drivers and strength of bathymetric self-organization. *Journal of Geophysical Research: Oceans*, *130*, e2024JC021726. https://doi.org/10.1029/2024JC021726

Received 16 AUG 2024
Accepted 24 DEC 2024

Author Contributions:
Conceptualization: Kyle M. Straub
Data curation: J. Kevin Reece, Kyle M. Straub
Formal analysis: J. Kevin Reece, Kyle M. Straub
Investigation: J. Kevin Reece, Kyle M. Straub
Methodology: J. Kevin Reece, Kyle M. Straub
Project administration: Kyle M. Straub
Resources: Kyle M. Straub
Supervision: Kyle M. Straub
Visualization: J. Kevin Reece, Kyle M. Straub
Writing – original draft: J. Kevin Reece
Writing – review & editing: Kyle M. Straub

Statistics of Depressions Covering the Northern Gulf of Mexico Salt-Minibasin Province: Drivers and Strength of Bathymetric Self-Organization

J. Kevin Reece[1] and **Kyle M. Straub**[1]

[1]Department of Earth and Environmental Sciences, Tulane University, New Orleans, LA, USA

Abstract The bathymetry of the northern Gulf of Mexico is strongly influenced by diapirism of subsurface salt. A competition between salt dynamics and the depositional mechanics of sediment laden density flows over geological timescales controls the scale of seafloor depressions, which are the dominant bathymetric features of the margin. Salt domes create topographic highs, and salt removal to the domes creates topographic lows, with sediment deposition driving the gravitational dynamics. The strength of bathymetric self-organization into depressions is inferred through analysis of a vast bathymetric data set made public by the U.S. Bureau of Ocean and Energy Management. Depression geometric scales follow Pareto distributions, and their tail indexes aid inference of the strength of bathymetric self-organization, with lower tail indexes linked to greater self-organization. A comparison is made of margin subregions defined by pseudo-flow drainage density maps, which inversely relates to the pre-deformation thickness of subsurface salt. Tail indexes of distributions decrease with the thickness of the underlying salt. This is linked to the merger of depressions, which is enhanced when depressions can grow wider and deeper, as occurs over thick salt fields, and the development of salt structure. The manner of self-organization results in most of the margin's ponded sediment accommodation residing in relatively few depressions that have reliefs exceeding 100 m. This relief is sufficient to induce sedimentation from even the thickest turbidity currents, which can further drive gravitational dynamics. The bathymetric complexity of depressions is also greatest over regions with the thickest salt, further supporting enhanced self-organization.

Plain Language Summary Below the seafloor of the northern Gulf of Mexico resides a thick salt layer, which over geological timescales moves as a fluid in response to the deposition of sediment from above. Movement of this salt produces seafloor domes and depressions of a range of sizes. This study quantifies the size of seafloor depressions on the continental slope of the northern Gulf of Mexico. This is accomplished using a map of seafloor topography generated by the U.S. Bureau of Ocean Energy Management. Distributions of depression sizes indicate that more large depressions are found on the margin than would be expected from common distributions classes (e.g., exponential or Gaussian distributions). This suggests that due to salt migration, small depressions merged with one another to generate larger depressions, which is a type of self-organization. Seafloor depressions have the potential to slow the downslope movement of sediment avalanches called turbidity currents, which could cause sediment deposition and the filling of depressions. Our results suggest that the largest depressions on the margin also produce most of the ponded space to store sediment on the margin. The scales of these depressions are also large enough to induce sedimentation from almost all turbidity currents.

1. Introduction

In both terrestrial and marine environments, a morphodynamic feedback system exists, composed of topography, fluid flow, and sediment transport. These three parameters collectively control the morphology of sediment routing systems. In discussions of this feedback system, topographic adjustments generally focus on sediment exchange with a sediment covered bed (Church, 2006; Jerolmack & Mohrig, 2005; McElroy & Mohrig, 2009; Naden, 1987; Simpson & Schlunegger, 2003; Smith & McLean, 1977). Each component of this morphodynamic feedback system directly influences the other two components; for example, a reduction in transport slope with downstream distance induces a reduction in flow velocity and thus sediment transport capacity, resulting in deposition and alteration of the slope. The gradient of many continental slopes is a direct product of this morphodynamic feedback system, where the dominant sediment transporting flows are turbidity currents (Pratson et al., 2007; Pratson & Haxby, 1996). While some continental margins exhibit relatively simple concave up profiles, others display significant bathymetric complexity (Mosher et al., 2017; Prather, 2003; Pratson & Haxby, 1996; Thorne & Swift, 1992). This complexity includes nested depressions, or depressions within depressions. The concept of a morphodynamic feedback system takes on new meaning in settings underlain by salt or uncompacted shale as sediment loading, controlled by sediment supply, can cause ductile substrate deformation over geological timescales, which continues to influence the fluid and sediment transport fields. This deformation contributes to deviations from the geological concept known as grade, which in terms of sedimentary dynamics represents the equilibrium profile of a margin, shaped by sediment-transporting flows in the absence of time-varying subsidence or uplift (Gilbert, 1877; Mackin, 1948; Prather, 2003). This equilibrium state results from a balance of sedimentation with the production of accommodation. Here, accommodation is the space available to store sediment below grade, and is formally defined in a volumetric framework (Jervey, 1988). Quantifying accommodation is analogous to detailing the instantaneous potential for change in an evolving continental margin. While the concepts of grade and accommodation have been around for decades, few studies characterize the statistics that describe how accommodation is organized on continental margins that results from mobile substrates deforming over geological timescales.

Following prior research (Prather, 2003), we recognize a type of accommodation, termed ponded accommodation, as the space lying within three-dimensionally closed topographic lows on continental slopes whose cap is defined at the height of the lowest spill point. Ponded accommodation is highly effective at extracting sediment from turbidity currents as they must traverse flat and/or adverse slopes, which decelerate flows and reduce sediment transport capacity (Lamb et al., 2006; Patacci et al., 2015). Depressions resulting from diapirism and formation of other structures on salt canopies form intraslope basins that are large enough to influence the depositional mechanics of turbidity currents are often termed minibasins by geologists working the Gulf of Mexico (GoM). Numerical and physical experimental studies suggest minibasins can cause collapse of turbidity currents, or in some cases induce hydraulic ponding and flow inflation (Bastianon et al., 2021; Dorrell et al., 2018; Lamb et al., 2004; Patacci et al., 2015; Reece et al., 2024) Hydraulic ponding, a process where flows are trapped within depressions, initiates when turbidity currents reflect off distal depression walls. Ponding generates low densimetric Froude number flows with limited ambient fluid entrainment and usually requires depression relief to be comparable to the thickness of a turbidity current (Lamb et al., 2004; Patacci et al., 2015; van Andel & Komar, 1969).

Here, the statistics of minibasins along the northern Gulf of Mexico are quantified to understand the scales of depressions that are important for this type of accommodation. For example, does ponded accommodation predominantly exist in a few large minibasins or in smaller depressions, of which there are many. Additionally, distributions of depressions geometric scales offer insights into the self-organization of bathymetry and how this self-organization changes as either a function of water depth or original thicknesses of subsurface salt. Given the scales of depressions on the margin and the complexity of the subsurface geology (Hudec, Jackson, & Peel, 2013; Kilsdonk et al., 2010; Pilcher et al., 2011), we envision this self-organization occurring over the geological timescales (i.e., >1 Myrs).

Organization of depressions through movement of subsurface salt has been inferred by imaging of strata beneath and around minibasins that suggest patterns of minibasin subsidence can be influenced by neighboring minibasins (Hudec et al., 2009) if they develop sufficiently close to one another. This is supported by dynamics captured in numerical and physical experiments, in which strata can be rotated due to spatial variations in the salt flow field, inducing temporal and spatial gradients in minibasin floor subsidence (Callot et al., 2016; Fernandez et al., 2020). Given the spatial configuration of sediment loading, these interactions can even lead to depression merger through time, resulting in aerially extensive minibasins. In addition to depression merger, the size and location of depressions (specifically the larger depressions) has been linked to the structure of allochthonous Sigsbee salt canopy (Kilsdonk et al., 2010; Pilcher et al., 2011). We emphasize that this subsurface salt structure is also partially the result of sediment loading over the evolution of the GoM and thus is part of the self-organization of bathymetry.

We ask how the statistics of depressions change (a) along an east to west transect that runs roughly parallel to the regional slope from thin to thick and back to thin subsurface salt and (b) as a function of water depth. This quantification helps define the roughness scales that turbidity currents interact with as they move down the GoM margin. These roughness elements slow the downslope progression of turbidity currents resulting in sediment deposition that fills accommodation, bringing the margin closer to grade (Alexander & Morris, 1994; Mackin, 1948; Nasr-Azadani & Meiburg, 2014; Soutter et al., 2021). Deposition then further drives the unique morphodynamic feedback system of salt provinces as the resulting deposition has the potential to induce further salt withdrawal and minibasin subsidence.

2. Background

2.1. Bathymetric Impacts of Mobile Salt Substrates

Gravity-driven salt diapirism plays a crucial role in shaping the geomorphology of the passive northern GoM continental margin (Worrall & Snelson, 1989). In regions underlain by mobile salt substrates, differential sediment loading can cause ductile substrate deformation over geological timescales (Gemmer et al., 2004; Schultz-Ela et al., 1993). This deformation results in the upward migration of salt bodies, leading to the formation of salt domes and canopies (Peel, 2014). Horizontal salt movement can be driven by pressure gradients, governed by the competition between Couette and Poiseuille flows along compressional margins (Ings & Beaumont, 2010). Ultimately, mobile salt influences seafloor geomorphology that feeds back on the fluid and sediment transport fields of turbidity currents (Peel, 2014; Reece et al., 2024).

2.2. Geologic Setting: Northern Gulf of Mexico

The history of the GoM basin is analogous to other passive margins underlain by thick salt deposits that date to the early Mesozoic era, such as those found in the South Atlantic salt basins, Red Sea, and southern Moroccan/Scotian margins (Rowan, 2022). During this time, fault bounded basins formed across what is now a 400 km wide zone, resulting from the rifting of the supercontinent Pangaea (Pindell & Dewey, 1982). Salt deposition began around 160 million years ago (Ma), giving rise to the Louann Salt formation (Bird et al., 2005). Prior to deformation, the Louann Salt was estimated to be at least 3–4 km thick near its center (Hudec, Norton, et al., 2013), corresponding to the present-day Fill and Spill region of the northern GoM minibasin province. The formation stratigraphically pinches out toward the eastern and western basin boundaries (Hudec, Norton, et al., 2013; Salvador, 1991; Steffens et al., 2003). Movement of the Louann Salt controls much of the region's modern topographic variations and complexity (Andrews, 1960; Hudec, Jackson, & Peel, 2013).

Sediment influx from the hinterland played a crucial role in shaping the evolution of Louann Salt into its current configuration (Jackson & Seni, 1983). Density contrasts between the encapsulated salt and the surrounding clastic sediment matrix generated buoyant forces, facilitating upward salt mobility (Martinez, 1991). Salt migration was not purely vertical, but also occurred laterally (Ings & Beaumont, 2010). This lateral migration was driven by a combination of salt evacuation beneath zones of sediment deposition (Gemmer et al., 2004), associated pressure differentials (Ings & Beaumont, 2010), and gravitational forces that moved much of the salt down dip toward the Sigsbee Escarpment (Humphris Jr, 1979).

Many rivers transport sediment from the terrestrial to the ocean along the northern GoM margin, the largest being the Mississippi River, which transports a sediment load of 210 million metric tons per year to the northern GoM (Blum & Roberts, 2009). A summation of the modern loads of the largest nine rivers suggests an approximate delivery of 234 million metric tons per year to the northern GoM (Milliman & Syvitski, 1992). Much of this sediment is deposited on the continental shelf but may be delivered through turbidity currents to canyons that dissect the continental slope and to open slope settings, with significant episodes of slope sediment deposition occurring over the last 160 Ma (Galloway, 2008). While much of sediment delivered to the slope by the Mississippi River is funneled down canyon systems (Galloway et al., 2000), sediment supplied by the smaller coastal systems helps construct shelf-edge deltas and delivers sediment to the upper continental slope.

At present, much of the Louann Salt is allochthonous, or moved from its original state and emplaced above stratigraphically younger strata (Wu et al., 1990), and is relatively thin along the northern portion of the continental margin. The Louann Salt thickens in the direction of the Sigsbee Escarpment, which is the leading edge of the migrating salt (Slowey et al., 2003). As the Louann Salt flowed and deformed, it formed localized accommodation for sediment deposition, some of which are now the targets for geofluid exploration (e.g., hydrocarbons in their gas and liquid forms, as well as CO_2, and water; see Mohriak et al., 2012; Stricker et al., 2018; Prather, 2003). Many of the large modern minibasins appear to have sunk into structural lows in the base of the salt canopy (Pilcher et al., 2011).

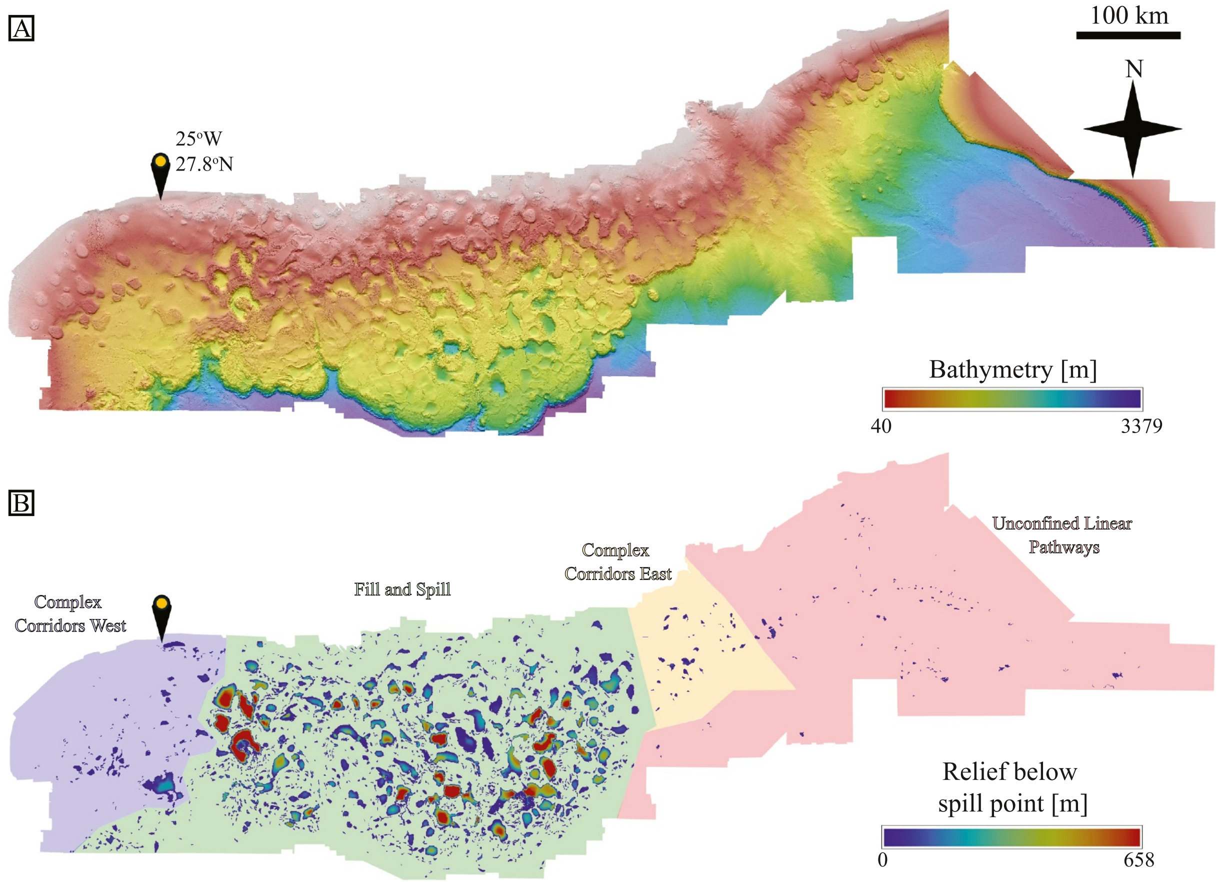

Figure 1. (a) BOEM's northern Gulf of Mexico deepwater bathymetry data set (Kramer & Shedd, 2017), displayed with WGS84 projection. The data set is a grid created from 3D seismic surveys and is comprised of 1.4 billion 12.19-by-12.19 m cells. Shaded relief overlays colored bathymetry and is vertically exaggerated by a factor of five. (b) ArcGIS Pro extracted local depressions with their shaded relief (polygons) in the northern GoM using BOEM's bathymetry data set. The data set covers much of the northern GoM continental margin with much of it underlain by the Louann Salt mobile substrate. Four regions (colored) follow those outlined by Steffens et al. (2003), as they overlap with the BOEM bathymetry data set.

Regional mapping shows that most of the mature minibasins are salt welded, indicating that they cannot sink further into the underlying salt and can no longer create additional ponded accommodation because pressure gradients have caused all the salt beneath subsiding minibasins to be evacuated (Colling et al., 2001; Galloway, 2008; Hudec, Jackson, & Peel, 2013; Ings & Beaumont, 2010). These mature minibasins dominantly occur on the upper slope in the central portion of the minibasin province of the northern GoM, here termed the Fill and Spill region. Additionally, mapping the top of salt within this Fill and Spill region suggests that salt welded minibasins occur more often on the continental slope, closer to the continental break and the sediment supply off shelf-edge deltas, than toward the Sigsbee Escarpment (Colling et al., 2001). This is linked to muted topography across the upper slope of the central minibasin province as mud belts from shelf-edge deltas can heal minibasin topography without further salt withdrawal subsidence. This allows slope profiles to form that are nearly the same grade as the unconfined eastern GoM slope.

3. Data and Methods

3.1. BOEM Bathymetry Data Set

This study leverages a bathymetric data set of 1.4 billion cells that are 12.19 × 12.19 m (Figure 1) (Kramer & Shedd, 2017). This data set was created by the Bureau of Ocean and Energy Management (BOEM) using a mosaic of 3-D seismic surveys over a 233,099 km^2 region and has an average vertical error of 1.3% of water depth, *WD*, which ranges from 40 to 3,380 m. The data set was used to extract minibasin reliefs, planar surface areas, and volumes across the entire northern GoM margin and then for subregions of the margin (Figure 1). Prior quantification of ponded accommodation on the northern GoM margin by Steffens et al. (2003) used a bathymetric map with a 200–250 m node spacing, thus a resolution ∼16–20 times coarser than the BOEM data set.

3.1.1. Definition of Subregions Along a Slope-Parallel Transect

The primary goal of this study is to characterize distributions of depression geometry over a wide range of scales and to quantify the complexity of these depressions. To achieve this, we quantify and compare accommodation statistics in four subregions of the northern GoM margin. Steffens et al. (2003) defined these subregions through analysis of a drainage density map. This map was produced by a drainage path analysis that routes pseudo-flow down steepest paths of descent. These four subregions correlate with Louann Salt substrate thicknesses and are presented here by decreasing underlying salt thicknesses: Fill and Spill, Complex Corridors, and Unconfined Linear Pathways (Figure 1) (Steffens et al., 2003). Here, the seafloor character of these subregions is attributed to underlying salt dynamics driven by differential sediment loading (Gemmer et al., 2004), and pressure gradients resulting from lateral salt sheet movement in a compressional toe-of-slope environment (Ings & Beaumont, 2010). Movement of the mobile Louann Salt is largely responsible for the length and complexity of drainage pathways (Steffens et al., 2003). The Fill and Spill subregion is defined by drainage pathways that are generally <20 km long before terminating in local depressions. These paths often cluster within and near individual salt withdrawal intra-slope basins. Flanking the Fill and Spill subregion is the Complex Corridors West and Complex Corridors East subregions. These are characterized by more continuous but complex drainage corridors, with maximum dip extents of ∼60 km; similar to Smith's (2004) "connected tortuous corridors." East of the Mississippi Canyon, Steffens et al. (2003) defined an Unconfined Linear Pathway subregion that contains dip-oriented drainage paths up to ∼130 km in length. This drainage texture occurs in a graded unconfined slope setting with little or no salt substrate.

To assess the importance of the exact boundaries drawn by Steffens et al. (2003), we investigate how adjusting boundary locations between the four subregions alters the statistical analyses. This is accomplished with two adjustment scenarios. For the first scenario, the Fill and Spill regional boundaries are expanded by 50 km (>> typical minibasins diameters) to ensure the sampling of additional minibasins over the thickest region of salt, while all other regions are shrunk. The Fill and Spill region is centrally located, sharing boundaries with all other regions making it a prime candidate to alter all boundaries for additional analyses. For the second scenario, the Fill and Spill regional boundaries are shrunk by 50 km, while all other regions are expanded.

3.1.2. Definition of Subregions Defined by Water Depth

Given the gravitationally driven movement of the Louann Salt toward the south, with the leading edge at the Sigsbee Escarpment in ultra-deep water, this study explores how the statistics of seafloor depressions vary as a function of water-depth. Specifically, we define four water depth bins, 57–1,000 m, 1,001–1,600 m, 1,601–2,000 m, and 2,001–3,379 m and compare statistics between bins. Note, these depth ranges are not uniform, but rather were selected to visually capture a similar number of depressions for comparison purposes. Placement of depressions into one of the four water depth bins is based on the maximum bathymetry (lowest elevation) of a depression.

3.2. Primary Depression Extraction

The full BOEM bathymetric data set was used to quantify distributions of depression geometric scales. An ArcGIS Pro Sink geoprocessing function (Mark, 1988) was employed to identify and extract sinks (topographic lows) within the raster data set. Sinks were identified by detecting bathymetric lows and expanding upward and outward in search of a spill point. Sinks were extracted from the raster data set with areas greater than 1 km^2 and maximum reliefs exceeding 5 m. The area cutoff value was set to be much more than the area of an individual pixel, and thus avoid apparent depressions that result from pixel-to-pixel error in the BOEM map. The 5 m relief cutoff value is less than the absolute vertical resolution of much of the data set, reported as 1.3% of water depth (Kramer & Shedd, 2017). However, most of this error is associated with merging seismic data sets collected in different years by different geophysical companies, resulting in cross-survey offsets. As a result, accuracy varied between surveys, but within survey precision is generally well below 1.3%. Given that most depressions are contained within the footprint of individual seismic surveys, geometric statistics can generally be accurately estimated for depressions with reliefs less than the reported absolute bathymetric error. Post-extraction analysis suggests consistent probability scaling of depression geometry begins for depressions larger than the 5 m limit, which we take as an indication of precision in defining geometry statistics.

The ArcGIS Pro Sink function identifies maximum depths within neighboring cells that have higher elevations. Next, a filling process occurs to determine the maximum area of each identified depression, which is set by the planar area contained below the depression spill point (Planchon & Darboux, 2002). Outputs from this sink extraction process are polygons that cover the surface area of each local depression (Mark, 1988). Lastly, bathymetric data underlying each of the polygons was saved as a raster file, allowing bathymetry to be analyzed for volumetric calculations below each surface area polygon. Extracted depressions were then sorted into subregions. The Steffens et al. (2003) subregions were replicated in ArcGIS Pro as polygons that overlap the extent of the BOEM bathymetry data set (Figure 1) allowing depressions to be tied to subregions. Geometric statistics are generated for: (a) Maximum relief, defined as the greatest vertical relief between the depression floor and spill point, (b) planar nominal diameter, defined as the average diameter of the horizontal surface resulting from a filled depression, and calculated as:

$$D = 2\sqrt{\frac{A}{\pi}}, \tag{1}$$

where A is the planar surface area of a depression, (c) planar surface area, defined as the area of the horizontal surface resulting from a filled depression, and (d) ponded volume, defined as the volume between the seafloor and the horizontal surface resulting from a filled depression.

3.2.1. Depression Density Calculations

To compare the abundance of depressions between subregions, a depression count was made for each of the Steffens et al. (2003) subregions. A comparison of depression density, DD, between regions was accomplished with three methods. The first normalized depression counts, nD, by the planar area of a subregion, $A_{\text{subregion}}$

$$DD_{\text{normalized}} = \frac{n_D}{A_{\text{subregion}}}, \tag{2}$$

and as such did not factor in the planar area of individual depressions. The second method calculated the fraction of a region covered by enclosed depressions, R_{fc}, by summing all depression planar surface areas in a subregion, A_p, and dividing by the subregion's planar area, $A_{\text{subregion}}$,

$$R_{fc} = \frac{\sum_{i=1}^{n} A_{p_i}}{A_{\text{subregion}}}. \tag{3}$$

3.2.2. Ponded Accommodation Statistics

A final method to compare the density of depressions in subregions calculates the average thickness of ponded accommodation in a subregion, PA_{at}, by summing the ponded accommodation of all depressions in a subregion, PA, and normalizing by the subregion's planar area.

$$PA_{at} = \frac{\sum_{i=1}^{n} PA_i}{A_{\text{subregion}}}. \tag{4}$$

Next, to quantify the importance of large versus small depressions in the total ponded accommodation of a region, plots of the fraction of a subregion's ponded accommodation (a function of primary depression volumes, V_D) residing in depressions that exceed a given maximum relief, R,

$$F_A(R > r) = \frac{\sum_{i=1}^{n} V_{D_i}(R > r)}{\sum_{i=1}^{n} V_{D_i}}, \tag{5}$$

nominal planar diameter, D,

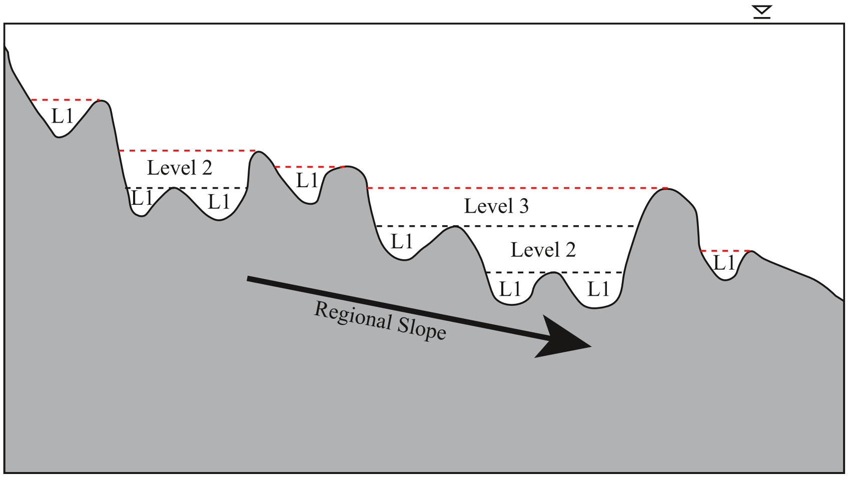

Figure 2. Schematic diagram showing topographic nested level hierarchy of seafloor depressions. Black dotted lines represent spill point heights for each level. Red dotted lines indicate primary depressions that contain lower nested level depressions. Level 3 is the highest level in this schematic with the lowest hierarchy the base Level 1 depressions. Regional slope is from left to right and is annotated as an arrow on the schematic diagram. Note: Level 1s are abbreviated as "L1" on the diagram.

$$F_A(D > d) = \frac{\sum_{i=1}^{n} V_{D_i}(D > d)}{\sum_{i=1}^{n} V_{D_i}}, \tag{6}$$

area, A,

$$F_A(A > a) = \frac{\sum_{i=1}^{n} V_{D_i}(A > a)}{\sum_{i=1}^{n} V_{D_i}}, \tag{7}$$

and/or volume, V,

$$F_A(V > v) = \frac{\sum_{i=1}^{n} V_{D_i}(V > v)}{\sum_{i=1}^{n} V_{D_i}}, \tag{8}$$

are generated. This analysis was also conducted for the full northern GoM data set.

3.2.3. Nested Depression Hierarchy

A nested-level hierarchy analysis was utilized to quantify the propensity for depressions to be nested within larger depressions, which is a proxy for topographic complexity. This analysis was completed for all subregions of the northern GoM. A Python package named Lidar (Wu, 2021), developed for terrestrial settings, was used to delineate nested level depressions from the ArcGIS Pro Sink raster output using a 5 m minimum depth, and a 5 m slicing interval (i.e., vertical spacing between successive layers used in analysis) (Wu, 2021; Wu et al., 2019). This algorithm follows a similar methodology to Le and Kumar (2014). First, base level depressions (lowest depressions in the hierarchy) are identified by the lowest elevation cells relative to their surrounding cells and tracked up to a localized rim with one cell acting as a spill point. Depressions below this spill point are considered Level 1 depressions (Figure 2). Two Level 1 depressions that share a common spill point merge above into a Level 2 depression. Level 2 depressions that share a spill point with other Level 2 or Level 1 depressions continue to grow up the hierarchy chain to become Level 3 depressions. The depression with the highest level of hierarchy is referred to as the "primary depression." This process continues until a regional spill point is reached, in which flow stripped from the upper portions of partially confined turbidity currents would descend the regional slope until another primary depression is reached (Figure 2).

Journal of Geophysical Research: Oceans 10.1029/2024JC021726

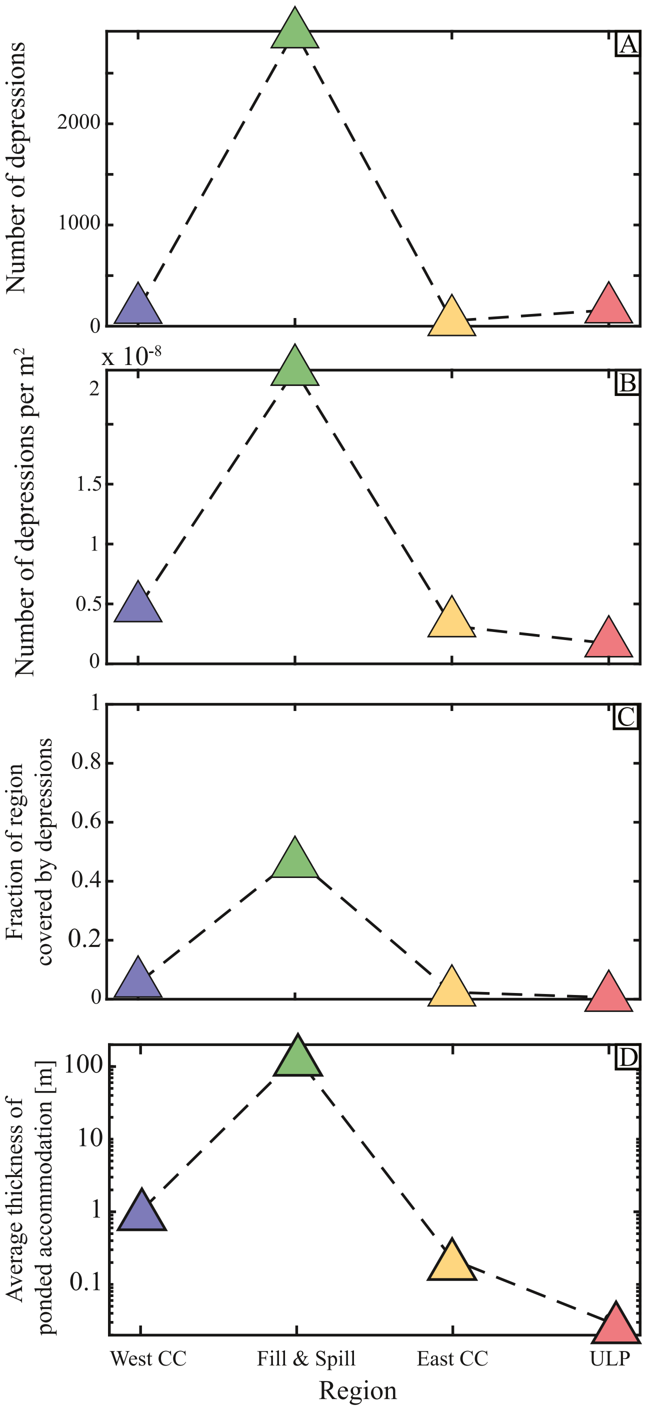

Figure 3. Plots showing regional variations of (a) number of depressions extracted, (b) number of depressions per m^2, (c) fraction of region covered by depressions and (d) average thickness of ponded accommodation in a region.

4. Results

4.1. Depression Densities

The Fill and Spill region has the largest number of primary depressions with a total count of 2,914, in a subregion with an area of 107,142 ± 498 km^2 (Figure 3), thus an approximate density of 2.45×10^{-2} depressions/km^2. Depression density decreases in the Complex Corridors Regions to the west (n = 163; 4.60×10^{-3} depressions/km^2) and east (n = 53; 3.17×10^{-3} depressions/km^2) of the Fill and Spill region. The Unconfined Linear Pathways region has 160 primary depressions, and the lowest depression density of 1.69×10^{-3} depressions per km^2 (Figure 3). Utilizing the planar areas of all depressions, the fraction of each subregion covered by depressions is estimated. This follows a similar, but accentuated, trend as the depression density. 45% of the Fill and Spill region is covered by depressions, decreasing to 5% and 2% in the West and East Complex Corridors regions, respectively. Finally, only 0.5% of the Unconfined Linear Pathway Region is covered by depressions (Figure 3c).

The average thickness of ponded accommodation highlights the ability of mobile salt beneath the Fill and Spill Region to generate significant space to store sediment (Figure 3d). The Fill and Spill region is on average covered by 136 m of ponded accommodation, which falls to between 0.2–1.0 m over the Complex Corridors regions and further down to only 0.03 m over the Unconfined Linear Pathways subregion (Figure 3d).

4.2. Depression Distributions

Probability of exceedance was calculated for maximum relief, nominal planar diameter, area, and volume of depressions. This was done first for the entire northern GoM, and then for each of the four subregions, and for each of the four water depth classifications (Figures 4 and 5). In all distributions, data follow an approximate log-log linear decay over most of the parameter space, which spans several decades for each geometric variable. This log-log linear decay transitions to an approximate exponential decay for extremely large depressions, when considering the full margin, the Fill and Spill region, or for all water depth ranges. However, the log-log linear decay is not perfect. For example, when considering the whole margin, a kink exists in the decay of all four geometric parameters (e.g., near 50 m for the depression relief distribution), with a higher power-law slope transitioning to a lower slope as depression scale increases, suggesting enhanced organization of large, relative to small, depressions at the scale breaks. While we observe evidence of this kink, we are unaware of a distribution class that contains two power-law scaling regimes and a truncation parameter. As such, this analysis characterizes the distribution shape using both a Pareto distribution and a truncated Pareto for all data sets.

Power-law distributions, which follow a log-log linear decay in the probability of exceedance of a random variable are a common occurrence in a wide array of natural phenomena, including earthquake magnitudes, sizes of cities, daily fluctuations in the size of financial market indexes, and biological populations (Bak & Tang, 1989; Clauset et al., 2009; Gabaix et al., 2003; Kagan, 2010; Newman, 2005; White et al., 2008). This distribution class can indicate underlying processes or mechanisms that give rise to rare but impactful entities or events (Pinto et al., 2012). The Pareto is a common power-law distribution, which is characterized by a probability of exceedance of the form

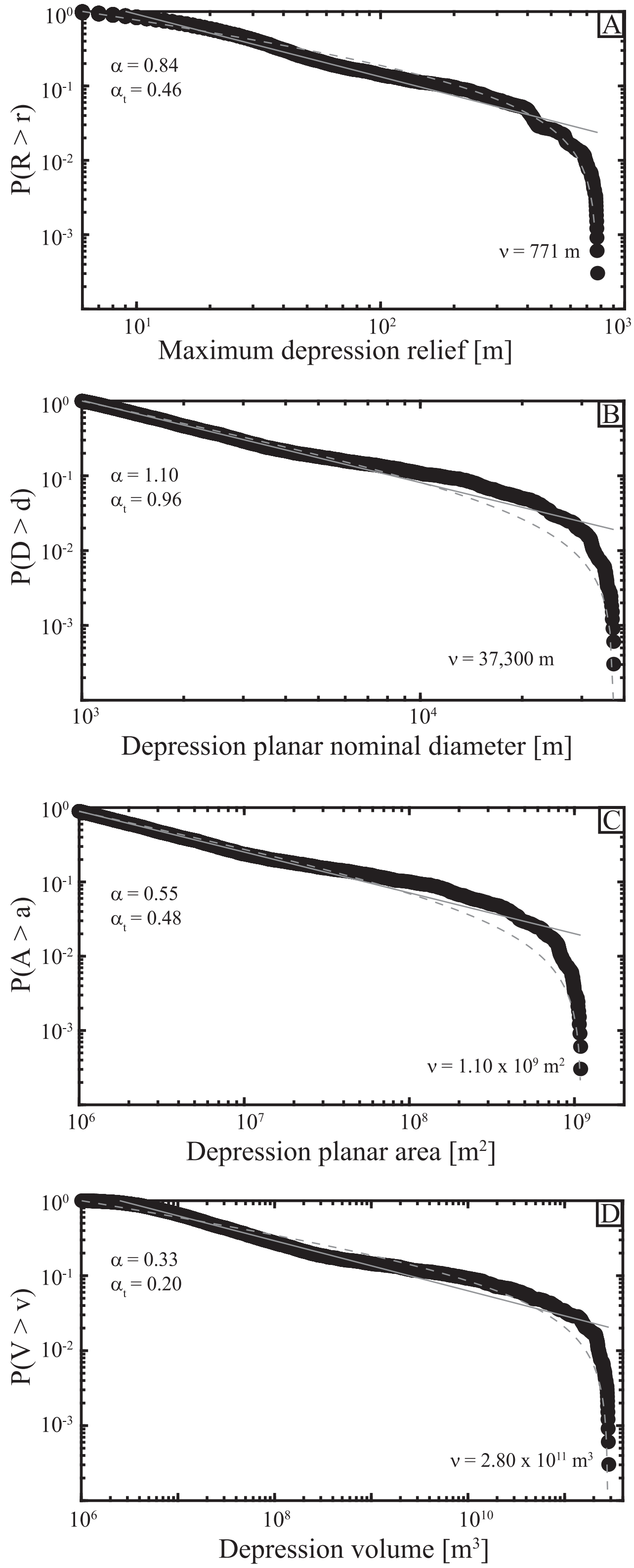

Figure 4. Plots showing probability of exceedance for depressions greater than a specific value for the full northern GoM depression data set, where (a) is maximum depression relief, (b) is nominal planar depression length, (c), is depression planar area, and (d) is depression volume. Note, the data set is plotted in log-log space, and both the fitted Pareto (solid lines) and truncated Pareto distributions (dashed lines) are overlayed.

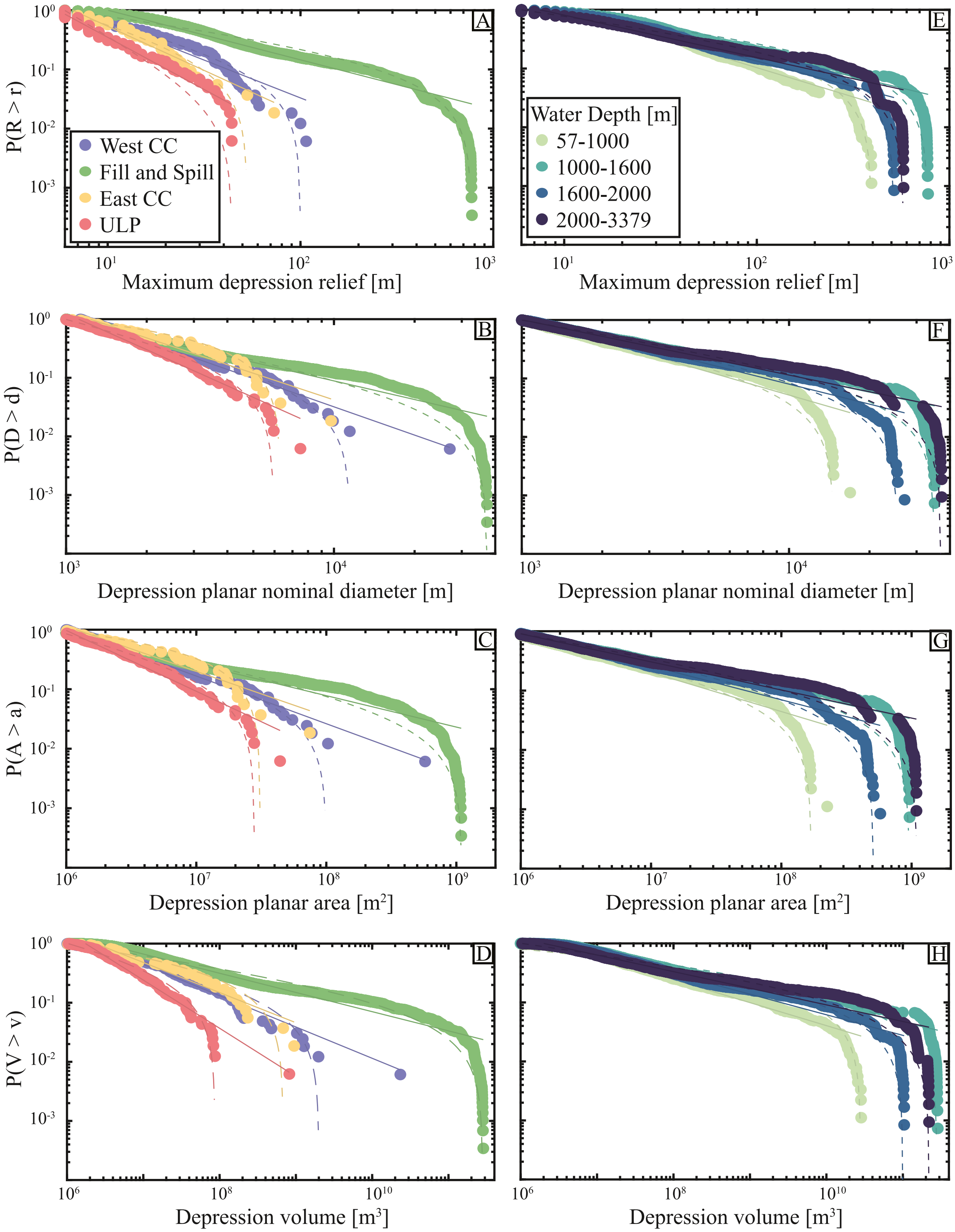

Figure 5. Plots showing probability of exceedance for depressions greater than a specific value for subregions along the west to east regional transect (a–d) or as a function of water depth (e–h), where (a, e) are for maximum depression relief, (b, f) are for nominal planar depression length, (c, g) are for depression planar area, and (d, h) are for depression volume. Note, data sets are plotted in log-log space and both the fitted Pareto (solid lines) and truncated Pareto distributions (dashed lines) are overlayed.

Table 1
Table Showing Estimated Parameters for Pareto and Truncated Pareto Fits for the Entire Northern GoM Data Set

	A	V	D	L
α	5.49×10^{-1}	3.34×10^{-1}	8.42×10^{-1}	1.10×10^{0}
γ	1.76×10^{-1}	1.37×10^{2}	6.37×10^{0}	2.02×10^{3}
Residual	9.08×10^{-1}	9.01×10^{-1}	8.69×10^{-1}	9.08×10^{-1}
$\alpha_{\text{truncated}}$	4.78×10^{-1}	1.98×10^{-1}	4.58×10^{-1}	9.57×10^{-1}
$\gamma_{\text{truncated}}$	7.86×10^{5}	1.01×10^{6}	6.00×10^{0}	1.00×10^{3}
υ	1.10×10^{9}	2.80×10^{11}	7.71×10^{2}	3.73×10^{4}
All Regions Data Set				

Note. A, Area; V, Volume; D, Depth; and L, Length. Row variables are defined in text.

$$P(X > x) = \left(\frac{\gamma}{x}\right)^{\alpha} \tag{9}$$

where x is the random variable, γ is the minimum possible value of the random variable, and α is the exponent of the power-law decay, also known as the tail index (Newman, 2005).

Results for the full margin, the Fill and Spill Region, and for all water depth ranges, suggest that at exceptionally large scales the probability of exceedance decreases with exponential trends (Figures 4 and 5), suggesting a finite size influence on the shape of the distribution. This trend can be well described by a truncated Pareto distribution of the form

$$P(X > x) = \frac{\gamma^{\alpha}\left(x^{-\alpha} - \nu^{-\alpha}\right)}{1 - (\gamma/\nu)^{\alpha}}, \tag{10}$$

where ν is the truncation parameter or the upper bound on the random variable, α is the tail index and γ is the lower bound on the random variable x (Aban et al., 2006; Ganti et al., 2011). Free parameters that define the Pareto and truncated Pareto fits were found using the maximum likelihood estimation method (Aban et al., 2006) (Figures 4 and 5, Tables 1 and 2).

A comparison of the tail index as a function of the dimensionality of the depression scale (maximum relief or nominal planar diameter [L], area [L^2], and ponded volume [L^3]) and subregion show the following trends. Generally, as the dimensionality of the scale increases, the tail index decreases (Figure 6). Tail indexes range from 1.06 to 2.05 for maximum depression diameters, which drops to 0.84–1.76 for depression reliefs, then down to 0.53–1.02 for depression areas, and then to 0.33–0.82 for depression volumes. Next, for all geometric scales, the Fill and Spill region has the lowest tail indexes, which increase as one traverses into the Complex Corridors Regions, and then into the Unconfined Linear Pathway subregion (Figure 6).

The tail index of a Pareto distribution carries significance for our ability to characterize the mean state of a random variable. When $\alpha > 2$, the distribution possesses a statistical mean (Newman, 2005). However, when $\alpha < 2$, a distribution lacks a statistical mean (Deluca & Corral, 2013), as the possibility of sampling a parameter of near infinite size is statistically significant. Distributions with tail indexes <2 are often discussed as having “heavy tails,” as extremely high parameter values are more probable than in a normal distribution (Kolmogorov & Bharucha-Reid, 2018). Truncated Pareto distributions with tail indexes <2 also are considered to possess heavy-tails, even though finite size effects prevent the sampling of near infinite values (Deluca & Corral, 2013). A key result here is the presence of $\alpha < 2$ in almost all dimensionality scales of the northern GoM depressions, which also occurs in all subregions and water depth ranges (Figures 4–6). Tail indexes reported above are from the standard Pareto distribution fits. However, we note that tail indexes generated from truncated Pareto fits are always less than those estimated from Pareto distributions (Table 2). Given that some of our distributions appear well fit by truncated Paretos, this further supports the characterization of most all geometric data sets as heavy-tailed.

Plots of the fraction of ponded accommodation housed in depressions exceeding a given scale (either maximum relief, planar diameter, area, or volume) highlight the importance of large depressions to the total ponded accommodation on this margin (Figure 7). Trends for all four parameters follow a very slow decay with increasing depression scales, but with very rapid fall-off at large depression scales. To highlight the importance of large depressions, we find that 90% of the ponded accommodation on the northern GoM margin resides in volumetrically the largest 147 of the 3,290 identified depressions. These depressions all have maximum reliefs greater than 273 m.

4.3. Nested Complexity

Quantification of depression nested complexity highlights potential relationships between depression scales and topographic complexity. The Fill and Spill region, which had the largest depression scales and heaviest distribution tails, stands out as the most complex. The depression with the most complexity in this region has 37 nested

Journal of Geophysical Research: Oceans

10.1029/2024JC021726

Table 2

Table Showing Estimated Parameters for Pareto and Truncated Pareto Fits Across Normal, Expanded, and Shrunken Sized Subregions, as Well as Four Water Depth Ranges, for the Entire Northern GoM Data Set

	A	V	D	L	A	V	D	L	A	V	D	L	A	V	D	L
α	8.01×10^{-1}	5.30×10^{-1}	1.28×10^{0}	1.60×10^{0}	5.28×10^{-1}	3.25×10^{-1}	8.39×10^{-1}	1.06×10^{0}	7.57×10^{-1}	5.10×10^{-1}	1.49×10^{0}	1.51×10^{0}	1.02×10^{0}	8.15×10^{-1}	1.76×10^{0}	2.05×10^{0}
γ	6.78×10^{4}	2.28×10^{3}	1.20×10^{1}	8.23×10^{4}	1.31×10^{3}	1.25×10^{2}	6.95×10^{0}	1.49×10^{3}	3.96×10^{4}	1.78×10^{3}	1.67×10^{1}	4.76×10^{4}	1.34×10^{6}	1.23×10^{5}	2.03×10^{1}	1.72×10^{6}
Residual	9.71×10^{-1}	9.22×10^{-1}	8.36×10^{-1}	9.71×10^{-1}	8.93×10^{-1}	8.88×10^{-1}	8.58×10^{-1}	8.93×10^{-1}	8.20×10^{-1}	8.62×10^{-1}	9.05×10^{-1}	8.20×10^{-1}	9.23×10^{-1}	9.25×10^{-1}	9.38×10^{-1}	9.23×10^{-1}
$\alpha_{truncated}$	6.02×10^{-1}	2.44×10^{-1}	7.93×10^{-1}	1.20×10^{0}	4.57×10^{-1}	1.81×10^{-1}	3.87×10^{-1}	9.13×10^{-1}	-3.78×10^{-2}	8.00×10^{-2}	8.93×10^{-1}	-8.45×10^{-2}	5.27×10^{-1}	2.67×10^{-1}	1.90×10^{0}	1.05×10^{0}
$\gamma_{truncated}$	9.90×10^{5}	9.89×10^{5}	5.96×10^{0}	1.12×10^{3}	7.85×10^{5}	1.05×10^{6}	6.00×10^{0}	1.00×10^{3}	8.08×10^{5}	9.33×10^{5}	5.89×10^{0}	1.01×10^{3}	7.78×10^{5}	1.03×10^{6}	5.98×10^{0}	9.96×10^{2}
υ	1.00×10^{8}	2.00×10^{9}	1.00×10^{2}	1.15×10^{4}	1.10×10^{9}	2.80×10^{11}	7.71×10^{2}	3.73×10^{4}	3.10×10^{7}	6.80×10^{8}	5.30×10^{1}	6.31×10^{3}	2.80×10^{7}	8.70×10^{7}	4.40×10^{1}	5.96×10^{3}
	Normal West CC				Normal Fill and Spill				Normal East CC				Normal ULP			
α	8.59×10^{-1}	6.54×10^{-1}	1.35×10^{0}	1.72×10^{0}	5.29×10^{-1}	3.28×10^{-1}	8.50×10^{-1}	1.06×10^{0}	8.13×10^{-1}	5.59×10^{-1}	1.53×10^{0}	1.63×10^{0}	1.05×10^{0}	8.15×10^{-1}	1.76×10^{0}	2.09×10^{0}
γ	1.19×10^{5}	1.41×10^{4}	1.47×10^{1}	1.46×10^{5}	1.36×10^{3}	1.32×10^{2}	6.93×10^{0}	1.54×10^{3}	8.16×10^{4}	3.41×10^{3}	1.65×10^{1}	9.93×10^{4}	1.82×10^{6}	1.19×10^{5}	2.02×10^{1}	2.34×10^{6}
Residual	9.64×10^{-1}	9.23×10^{-1}	7.25×10^{-1}	9.64×10^{-1}	8.93×10^{-1}	8.93×10^{-1}	8.64×10^{-1}	8.93×10^{-1}	7.84×10^{-1}	8.18×10^{-1}	8.20×10^{-1}	7.84×10^{-1}	9.35×10^{-1}	9.34×10^{-1}	9.35×10^{-1}	9.35×10^{-1}
$\alpha_{truncated}$	6.08×10^{-1}	1.65×10^{-1}	3.02×10^{-1}	1.21×10^{0}	4.48×10^{-1}	1.80×10^{-1}	4.16×10^{-1}	8.95×10^{-1}	-4.12×10^{-1}	-1.37×10^{-1}	3.63×10^{-1}	-8.52×10^{-1}	5.50×10^{-1}	2.83×10^{-1}	1.89×10^{0}	1.10×10^{0}
$\gamma_{truncated}$	7.80×10^{5}	1.23×10^{6}	5.90×10^{0}	9.97×10^{2}	7.85×10^{5}	9.98×10^{5}	6.00×10^{0}	1.00×10^{3}	8.89×10^{5}	8.04×10^{5}	5.76×10^{0}	1.06×10^{3}	7.78×10^{5}	1.03×10^{6}	5.98×10^{0}	9.96×10^{2}
υ	4.70×10^{7}	2.00×10^{8}	4.80×10^{1}	7.75×10^{3}	1.10×10^{9}	2.80×10^{11}	7.71×10^{2}	3.72×10^{4}	1.70×10^{7}	1.70×10^{8}	2.90×10^{1}	4.71×10^{3}	2.80×10^{7}	8.70×10^{7}	4.40×10^{1}	5.97×10^{3}
	Shrink West CC				Expand Fill and Spill				Shrink East CC				Shrink ULP			
α	7.74×10^{-1}	4.93×10^{-1}	1.15×10^{0}	1.55×10^{0}	5.47×10^{-1}	3.37×10^{-1}	8.69×10^{-1}	1.09×10^{0}	6.57×10^{-1}	4.24×10^{-1}	1.24×10^{0}	1.31×10^{0}	8.71×10^{-1}	5.26×10^{-1}	1.20×10^{0}	1.74×10^{0}
γ	3.61×10^{4}	1.37×10^{3}	1.19×10^{1}	4.35×10^{4}	1.72×10^{3}	1.52×10^{2}	7.52×10^{0}	1.96×10^{3}	9.37×10^{3}	5.02×10^{2}	1.11×10^{1}	1.10×10^{4}	1.71×10^{5}	1.97×10^{3}	8.18×10^{0}	2.12×10^{5}
Residual	9.95×10^{-1}	9.61×10^{-1}	8.56×10^{-1}	9.95×10^{-1}	9.02×10^{-1}	8.89×10^{-1}	8.38×10^{-1}	9.02×10^{-1}	9.19×10^{-1}	9.36×10^{-1}	9.21×10^{-1}	9.19×10^{-1}	9.55×10^{-1}	9.78×10^{-1}	9.50×10^{-1}	9.55×10^{-1}
$\alpha_{truncated}$	7.54×10^{-1}	3.24×10^{-1}	7.11×10^{-1}	1.51×10^{0}	4.69×10^{-1}	1.84×10^{-1}	3.62×10^{-1}	9.37×10^{-1}	2.79×10^{-1}	1.59×10^{-1}	7.64×10^{-1}	5.56×10^{-1}	6.09×10^{-1}	3.60×10^{-1}	1.21×10^{0}	1.22×10^{0}
$\gamma_{truncated}$	7.90×10^{5}	9.93×10^{5}	5.98×10^{0}	1.00×10^{3}	7.85×10^{5}	1.05×10^{6}	5.99×10^{0}	1.00×10^{3}	7.76×10^{5}	1.00×10^{6}	5.93×10^{0}	9.94×10^{2}	7.81×10^{5}	1.04×10^{6}	5.98×10^{0}	9.98×10^{2}
υ	8.40×10^{8}	2.30×10^{11}	5.86×10^{2}	3.27×10^{4}	1.10×10^{9}	2.20×10^{11}	5.77×10^{2}	3.72×10^{4}	1.20×10^{8}	3.50×10^{9}	9.60×10^{1}	1.23×10^{4}	1.80×10^{8}	1.90×10^{10}	2.08×10^{2}	1.51×10^{4}
	Expand West CC				Shrink Fill and Spill				Expand East CC				Expand ULP			
α	6.59×10^{-1}	3.90×10^{-1}	9.95×10^{-1}	1.32×10^{0}	4.80×10^{-1}	2.98×10^{-1}	7.78×10^{-1}	9.60×10^{-1}	5.68×10^{-1}	3.49×10^{-1}	8.72×10^{-1}	1.14×10^{0}	4.73×10^{-1}	2.82×10^{-1}	7.22×10^{-1}	9.47×10^{-1}
γ	8.30×10^{3}	3.18×10^{2}	1.01×10^{1}	9.70×10^{3}	6.99×10^{2}	8.79×10^{1}	6.40×10^{0}	7.85×10^{2}	2.45×10^{3}	1.90×10^{2}	7.40×10^{0}	2.80×10^{3}	6.27×10^{2}	5.96×10^{1}	4.28×10^{0}	7.03×10^{2}
Residual	8.70×10^{-1}	8.70×10^{-1}	8.30×10^{-1}	8.70×10^{-1}	8.60×10^{-1}	8.60×10^{-1}	8.30×10^{-1}	8.60×10^{-1}	8.80×10^{-1}	8.80×10^{-1}	8.50×10^{-1}	8.80×10^{-1}	8.60×10^{-1}	8.30×10^{-1}	8.00×10^{-1}	8.60×10^{-1}
$\alpha_{truncated}$	4.81×10^{-1}	5.68×10^{-2}	3.99×10^{-1}	9.62×10^{-1}	3.69×10^{-1}	1.37×10^{-1}	2.86×10^{-1}	7.37×10^{-1}	4.19×10^{-1}	1.65×10^{-1}	3.63×10^{-1}	8.38×10^{-1}	3.77×10^{-1}	1.64×10^{-1}	4.14×10^{-1}	7.54×10^{-1}
$\gamma_{truncated}$	7.86×10^{5}	1.64×10^{5}	5.99×10^{0}	1.00×10^{3}	7.85×10^{5}	9.96×10^{5}	5.99×10^{0}	1.00×10^{3}	7.84×10^{5}	1.07×10^{6}	5.99×10^{0}	1.00×10^{3}	7.84×10^{5}	1.04×10^{6}	5.99×10^{0}	1.00×10^{3}
υ	1.70×10^{8}	2.80×10^{10}	3.93×10^{2}	1.47×10^{4}	9.60×10^{8}	2.80×10^{11}	7.71×10^{2}	3.50×10^{4}	5.10×10^{8}	1.00×10^{11}	5.15×10^{2}	2.55×10^{4}	1.10×10^{9}	2.20×10^{11}	5.77×10^{2}	3.72×10^{4}
	Water Depth = 57–1,000 m				Water Depth = 1,001–1,600 m				Water Depth = 1,601–2,000 m				Water Depth = 2,001–3,379 m			

Note. A, Area; V, Volume; D, Depth; and L, Length. Row variables are defined in text.

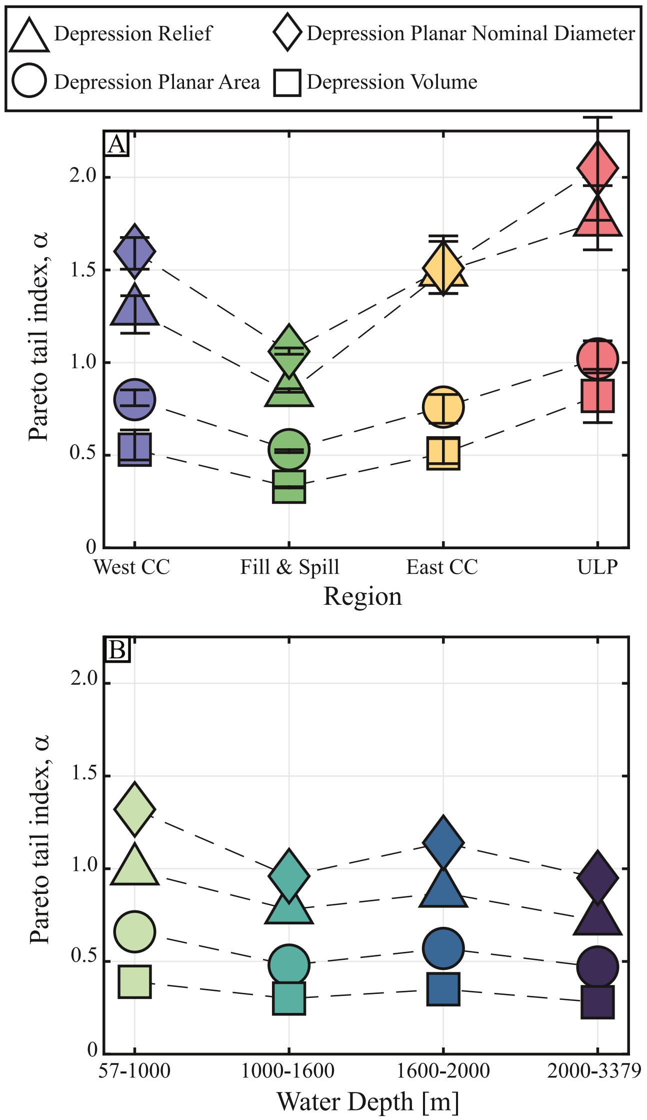

Figure 6. Data defining how power-law tail index (α) varies across (a) slope parallel transect and (b) for different water depth bins, which include relief, nominal planar diameter, planar area, and volume. Whiskers on error bars in subplot (a) represent minimum and maximum tail indexes for subregions based on the analysis of the expanded or shrunken subregions.

depression scales, a result that highlights that larger depressions typically have more hierarchical levels (Figure 8a). The Complex Corridors West region, which holds the second-highest degree of nested depression complexity, had a maximum of 11 level depression scales in a single primary depression. The Complex Corridors East region is characterized by a maximum of 5 level depression scales. The Unconfined Linear Pathways region has the least complexity of all subregions, with a maximum of 3 level depression scales.

Distributions of nested levels in depressions by subregion also follow power-law decay in probability of exceedance (Figure 8a) and these distributions in the Fill and Spill and Complex corridors have heavy tails (Figure 8b) with the lowest tail-index in the Fill and Spill subregion. Confirmation of distribution class is difficult for the Unconfined Linear Pathway subregion, as we observe a maximum of 3 nested levels, but the tail index for this region might be as high as 2.26.

5. Discussion

5.1. Basin Scale Ponded Accommodation

Large topographic depressions have the capacity to trap turbidity currents on their downslope traverse of continental margins (Lamb et al., 2006), inducing the accumulation and retention of sediment, nutrients, and pollutants (Galy et al., 2007; Kane et al., 2020; Talling et al., 2023). Results reveal that a significant portion of the ponded accommodation on the northern GoM is concentrated in a small subset of the very largest depressions. For example, 90% of the ponded accommodation on the margin resides in the deepest 147 depressions, which all have reliefs more than 273 m. This relief is likely sufficient to trap the largest turbidity currents that move down the GoM margin.

Ponding, which promotes sediment deposition, is thought to occur for flows that are capable of traversing the floor of minibasins and which have comparable thickness to the minibasin relief (Lamb et al., 2006). This creates a unique feedback as minibasins fill with sediment. During filling the width of low sloping minibasin floors increases, which can drive ponding of the mud component of turbidity currents, while the depositional mechanics of sand resemble unconfined conditions (Prather, 2020). While no active turbidity currents in GoM minibasins have been measured, turbidity currents have been recorded in other settings; for example, in the Monterey Canyon (Xu et al., 2004) and in the Zaire submarine channel (Talling et al., 2022). Recorded flows at these sites have not exceeded 60 m. Self-formed and aggradation channels along other margins, for example, Amazon (Pirmez & Imran, 2003) and Bengal (Kolla et al., 2012) submarine channels, can have reliefs in excess of 100 m, suggesting some flows that are at least this thick. Along the northern GoM margin, self-formed and aggradational channels up to 40 m deep have been observed entering or traversing minibasins (Panel B of Figure 10, Badalini et al., 2000). Experiments suggest that turbidity currents can have thicknesses that are 1.3 times the depth of the channel that is guiding them and still act as channelized flows (Mohrig & Buttles, 2007). Taken together, these findings suggest that most, if not all, flows that might interact with the current GoM minibasins will have thicknesses less than the relief of depressions that house most of the current ponded accommodation on the margin. Thus, most of the current ponded accommodation in the northern GoM has the potential to either cause turbidity currents to collapse or hydraulically pond, specifically for the muddy components of flows.

5.2. Bathymetric Self-Organization

A self-organized interplay between sediment loading, minibasin development, and salt mobility crafts the bathymetry of the northern GoM (Colling et al., 2001). Self-organized systems are ones linked to the spontaneous

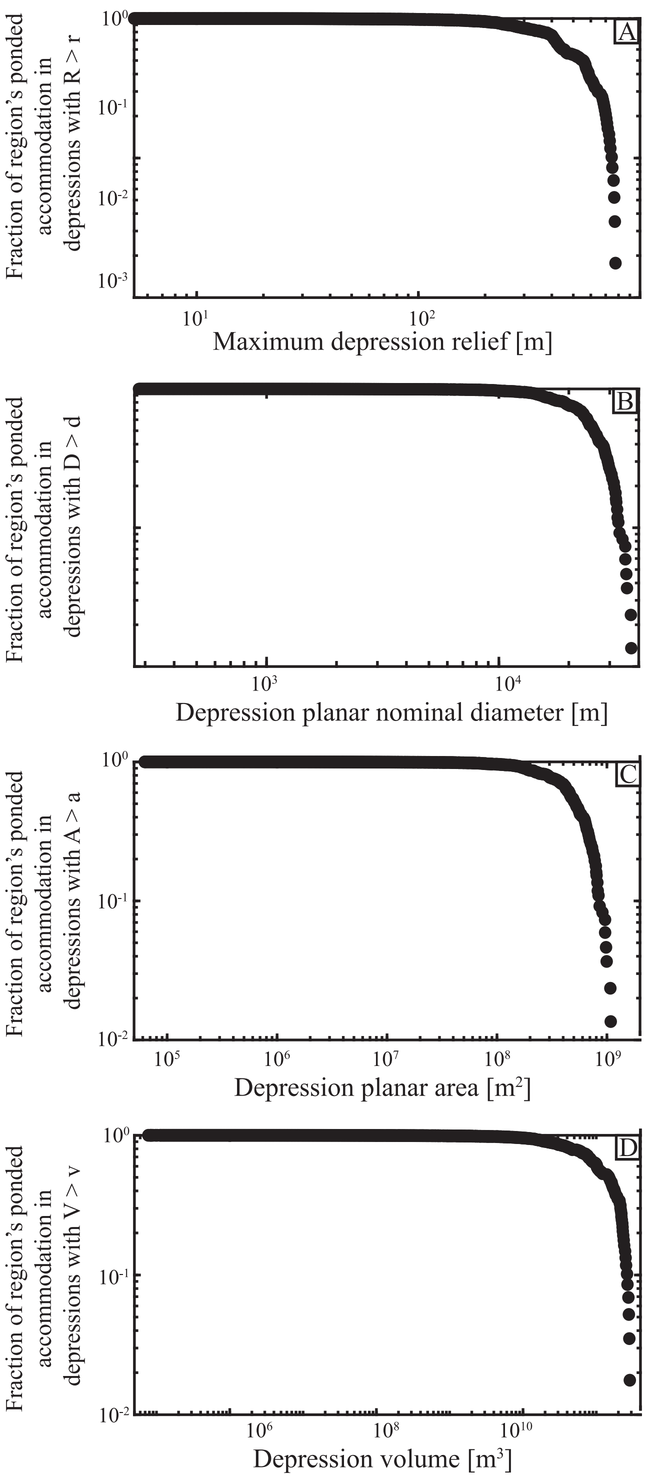

Figure 7. Fraction of northern GoM's ponded accommodation in depressions greater than a specific value for the full northern GoM data set, where (a) is maximum depression relief, (b) is nominal planar depression length, (c) is depression planar area, and (d) is depression volume.

emergence of a large-scale pattern through small-scale interactions between components of a system (Ashby, 1947; Hallet, 1990; Sornette, 2006). For salt-provinces, the pattern is the field of large-scale depressions (minibasins) that developed from differential loading of an initial salt sheet, where even minor spatial variations in loading or variations in initial salt thickness could set off a positive feedback loop where a change leads to further similar changes (Marković & Gros, 2014). As a result, some depressions grow faster than others, resulting in depression capture and spatially variable rates of salt convection and expulsion.

An attribute of self-organized systems is their resiliency to perturbations, linked to an ability to self-repair. This is attributed to external drives and internal dynamics competing on similar time scales (Marković & Gros, 2014). In the northern GoM, the external driver can be thought of as glacio-eustatic sea-level changes, resulting in depositional episodes on the slope that are sufficiently separated in time to allow for the salt to deform in response (Hudec & Jackson, 2007).

Bathymetric self-organization in salt provinces has been linked to the coalescence of hierarchically-scaled adjacent minibasins (Colling et al., 2001). While interaction of minibasins with one another has been hypothesized from subsurface imaging and explored in numerical and physical experiments (Callot et al., 2016; Fernandez et al., 2020), quantitatively linking these interactions to self-organization of the bathymetry is limited. However, self-organized systems often display power-law scaling of elements in the system, where the weight of the distribution tail is linked to the degree of self-organization (Marković & Gros, 2014). We highlight the relatively consistent decay in probability of the depression on geometric scales over several orders of magnitude, for example, 1–>10^3 km^2 for planform area (Figure 4). This consistent scaling suggests self-organization that is scale independent up to the truncation scale, or at least the lack of an obvious length scale that separates, for example, depressions which form from ductile salt flow from fault bound depressions. For minibasins, this self-organization can be thought of as follows: Coalescing of small-scale depressions into larger depressions redistributes probability within a distribution from small to large scales, in essence adding weight to the distribution tail. As such, the Pareto tail-index should inversely scale with the strength of self-organization in bathymetry toward larger depression scales. While depressions grow through deformation facilitated by ductile salt flow coupled with depression merger, it is worth highlighting that the largest depressions along the northern GoM are spatially located above structural lows in the underlying salt canopy, suggesting that deep structure impacts the specific location of the largest depressions and possibly their current size (Hudec, Jackson, & Peel, 2013).

We observe a change in self-organization from East to West across the northern GoM, but do not see a consistent change as a function of water depth (Figure 6; Table 2). More specifically, results herein suggest an increase in self-organization over the Fill and Spill subregion relative to neighboring subregions. This is due to the exceptionally low distribution tail-indexes over the Fill and Spill region, relative to all other regions.

Observations reported here support, but do not confirm, minibasin interaction and merger to form larger depressions. These observations add to previous studies that explored minibasin interactions, including findings from offshore Angola that show minibasins geometries suggestive of fossilized interactive dynamics in numerous two-way travel time structure maps and seismic sections (Ge et al., 2019). The merging of minibasins is thought to be closely tied to locations with thick

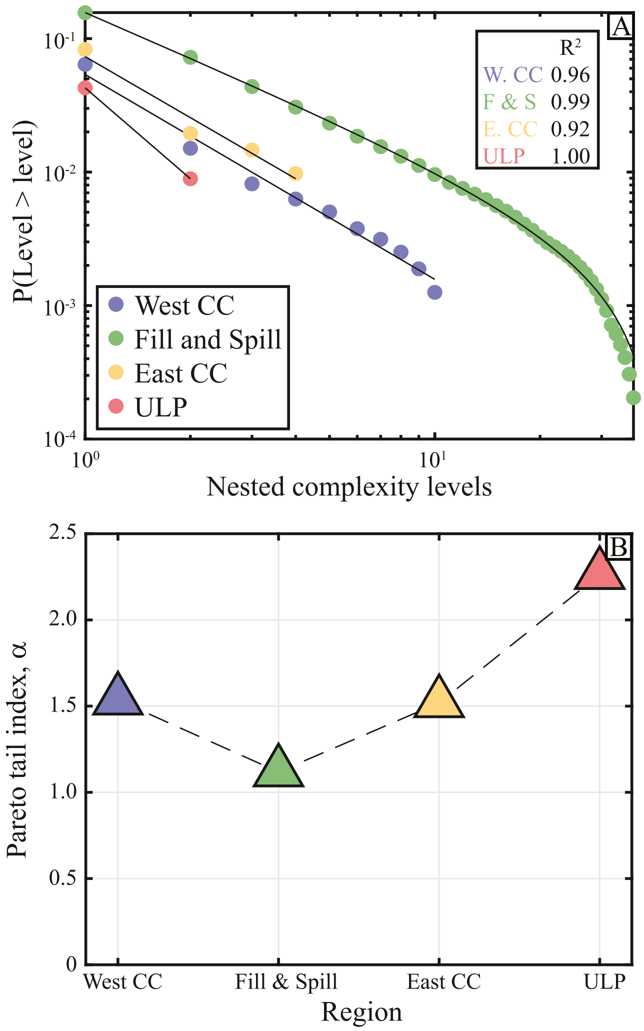

Figure 8. Plots show (a) probability of exceedance of nested depression levels and (b) tail indexes of probability of exceedance distributions for the four regions in the study.

underlying salt, likely due to the potential these conditions provide for localized salt movement and ultimately larger minibasin dimensions. Enhanced depression interaction and merging over the region with the greatest underlying salt thickness has direct implications for increasing the sediment trapping potential of minibasins, furthering the positive feedback loop. Not only are the tail-indexes less over the Fill and Spill subregion, but this region also has the largest and most complex depressions (Figure 8). A future avenue of research to confirm depression growth through merger in the northern GoM includes use of publicly available three-dimensional reflection seismic data. Case studies of specific minibasins might yield evidence frozen in the stratigraphic architecture of depression growth through merger.

The size of minibasins, for either the Fill and Spill subregion or the full margin, appear to be limited by a finite size effect (Figures 4 and 5). The upper limit on minibasin size is quantified by the truncation parameters (v) (Tables 1 and 2). We again highlight that the spatial location of the largest depressions in the GoM can be tied to the underlying structure of the salt canopy, which might support v being set by deep-seated salt structure (Hudec, Jackson, & Peel, 2013; Pilcher et al., 2011). However, we note the following: a global compilation of geometric data that describes lobe-shaped bodies (LBs), including lobe elements, lobes, and lobe complexes, in both unconfined and confined regions (Pettinga et al., 2018) show maximum LB area of approximately 10^9 m^2. This scale is approximately the truncation parameter for the depression area in our database. This suggests an alternate hypothesis to explain the magnitude of v. Specifically that v is set by the size of LBs that form from deposition of turbidity currents at the terminus of channels and load the margin in regions of sufficiently low slope to initiate turbidite deposition, coupled to sufficient subsurface salt that can be evacuated to generate a depression in response. If depressions grow with a self-similar form, then the area truncation scale would also limit the depression relief, nominal diameter, and volume distributions. This hypothesis is supported by physical experiments, where surface depression size rarely significantly exceeds the planform size of a sediment load placed on a proxy salt sheet (Callot et al., 2016). Support for a self-similar form of depression as a function of size can be found in an approximate linear growth of depression relief with diameter, with a best-fit scaling of relief being 0.014 times nominal diameter (Figure 9). However, we recognize difficulty in identifying the direction of the cause-effect relationship in this argument. For LBs to form, the margin's gradient must drop below grade, which leads to the following question. What process initially moved the margin out of grade? In the GoM, this might be linked to stepped Early Paleogene margin topography, which evolved into the current ponded slope (Galloway, 2008) due to early salt migration coupled with growth fault activity. In this scenario the initial size of depressions might be capped by the scale of the steps on the margin, if the step scale was less than the size of LBs in unconfined settings. Depressions then could evolve through time due to the depositional mechanics of unconfined turbidity currents and the subsurface salt dynamics. Alternatively, it might be coincidence that the maximum size of unconfined LBs is similar to the truncation scale of depression diameters and the maximum depression scale might be set by structural lows that evolved in the salt canopy (Kilsdonk et al., 2010; Pilcher et al., 2011).

5.3. Significance of Minibasin Size and Nested Complexity

Findings here suggest a correlation between minibasin size and nested complexity in the northern GoM, which is most noticeable in the Fill and Spill region (Figure 8). As the size of primary depressions increases, an increase in the number of nested levels is found. This suggests that turbidity currents must interact with multiple roughness scales within the largest minibasins. This increased complexity implies that sediment transport involving flows running up adverse slopes must frequently translate kinetic energy into potential energy, thus losing their

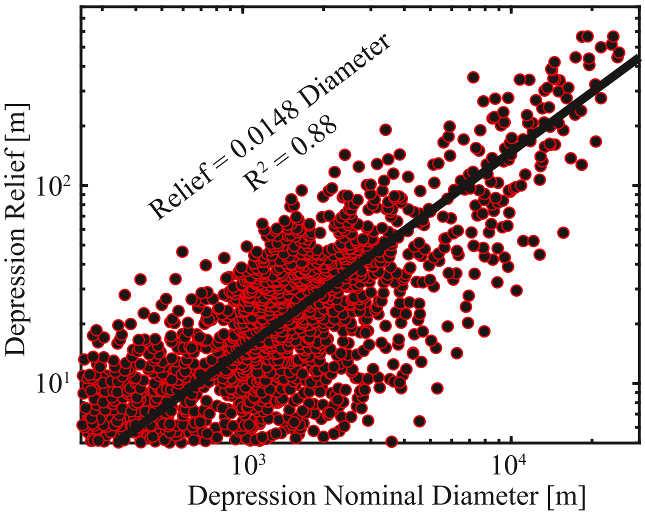

Figure 9. Scaling of depression nominal diameter to maximum depression relief.

sediment transport capacity. Adding more complexity (e.g., numerous counter slopes) leads to enhanced ponding of turbidity currents, and thus sedimentation processes, compared to cases where primary depressions consist of a single level of complexity.

6. Conclusions

This investigation of the northern GoM bathymetry quantifies distributions that describe the scales of depressions that house accommodation for sediment, with implications for depositional mechanics of turbidity currents and the self-organization of depression in salt provinces. Key findings include:

1) Results find that 90% of the ponded accommodation in the northern GoM resides in the volumetrically largest 147 of the 8,153 identified depressions, with maximum reliefs greater than 273 m. Most of the ponded accommodation in the northern GoM is capable of inducing deposition from the full range of turbidity current sizes that might flow down the northern GoM margin.
2) Self-organization of bathymetry in the northern GoM bathymetric data set is supported by heavy-tailed distributions of depression geometries. The weight of distribution tails, as quantified through Pareto tail-indexes, is greatest over the Fill and Spill region. This region was originally underlain by the thickest salt deposits. This suggests depression interaction over time, including depression growth through mergers. At the regional scale, these distributions are truncated, which suggests a finite size effect. We hypothesize that the maximum scale of turbidite lobes sets the truncation scales of minibasins.
3) The Fill and Spill region in the northern GoM reveals a clear association between minibasin size and nested complexity, with the largest minibasins exhibiting the greatest nested complexity. Turbidity currents entering the largest minibasins thus encounter a range of roughness scales, many of which are sufficient to induce hydraulic ponding of flows and reduce sediment transport capacity.

Data Availability Statement

Primary data used in this study is available at https://www.boem.gov/oil-gas-energy/mapping-and-data/map-gallery/northern-gom-deepwater-bathymetry-grid-3d-seismic.

Acknowledgments
We thank Mike Hudec, Brad Prather, and Giovanni Coco for reviews that significantly improved the manuscript. We also thank Editor Christopher Sherwood for shepherding this manuscript through the review process. We thank Vamsi Ganti for code to fit distributions. This research did not receive any specific grant from funding agencies in the public, commercial, or not-for-profit sectors.

References

Aban, I. B., Meerschaert, M. M., & Panorska, A. K. (2006). Parameter estimation for the truncated Pareto distribution. *Journal of the American Statistical Association*, *101*(473), 270–277. https://doi.org/10.1198/016214505000000411

Alexander, J., & Morris, S. (1994). Observations on experimental, nonchannelized, high-concentration turbidity currents and variations in deposits around obstacles. *Journal of Sedimentary Research*, *64*(4a), 899–909.

Andrews, D. I. (1960). The louann salt and its relationship to Gulf Coast salt domes.

Ashby, W. R. (1947). Principles of the self-organizing dynamic system. *The Journal of General Psychology*, *37*(2), 125–128. https://doi.org/10.1080/00221309.1947.9918144

Badalini, G., Kneller, B., & Winker, C. D. (2000). Architecture and processes in the late Pleistocene Brazos-Trinity Turbidite System, Gulf of Mexico continental slope. In P. Weimer, R. M. Slatt, J. Coleman, N. C. Rosen, H. Nelson, A. H. Bouma, et al. (Eds.), *Deep-water reservoirs of the world: Gulf Coast section SEPM foundation, 20th annual bob F* (pp. 16–34). Perkins Research Conference.

Bak, P., & Tang, C. (1989). Earthquakes as a self-organized critical phenomenon. *Journal of Geophysical Research*, *94*(B11), 15635–15637. https://doi.org/10.1029/jb094ib11p15635

Bastianon, E., Viparelli, E., Cantelli, A., & Imran, J. (2021). 2D numerical simulation of the filling process of submarine minibasins: Study of deposit architecture. *Journal of Sedimentary Research*, *91*(4), 399–414. https://doi.org/10.2110/jsr.2020.105

Bird, D. E., Burke, K., Hall, S. A., & Casey, J. F. (2005). Gulf of Mexico tectonic history: Hotspot tracks, crustal boundaries, and early salt distribution. *AAPG Bulletin*, *89*(3), 311–328. https://doi.org/10.1306/10280404026

Blum, M. D., & Roberts, H. H. (2009). Drowning of the Mississippi Delta due to insufficient sediment supply and global sea-level rise. *Nature Geoscience*, *2*(7), 488–491. https://doi.org/10.1038/ngeo553

Callot, J.-P., Salel, J.-F., Letouzey, J., Daniel, J.-M., & Ringenbach, J.-C. (2016). Three-dimensional evolution of salt-controlled minibasins: Interactions, folding, and megaflap development. *AAPG Bulletin*, *100*(9), 1419–1442. https://doi.org/10.1306/03101614087

Church, M. (2006). Bed material transport and the morphology of alluvial river channels. *Annual Review of Earth and Planetary Sciences*, *34*(1), 325–354. https://doi.org/10.1146/annurev.earth.33.092203.122721

Clauset, A., Shalizi, C. R., & Newman, M. E. (2009). Power-law distributions in empirical data. *SIAM Review*, *51*(4), 661–703. https://doi.org/10.1137/070710111

Colling, E. L., Alexander, R. J., & Phair, R. L. (2001). Regional mapping and maturity modeling for the northern deep water Gulf of Mexico. *Petroleum Systems of Deep-Water Basins: Global and Gulf of Mexico Experience: 21st Annual*, 87–110. https://doi.org/10.5724/gcs.01.21.0087

Deluca, A., & Corral, Á. (2013). Fitting and goodness-of-fit test of non-truncated and truncated power-law distributions. *Acta Geophysica*, *61*(6), 1351–1394. https://doi.org/10.2478/s11600-013-0154-9

Dorrell, R. M., Patacci, M., & McCaffrey, W. D. (2018). Inflation of ponded, particulate laden density currents. *Journal of Sedimentary Research*, *88*(11), 1276–1282. https://doi.org/10.2110/jsr.2018.65

Fernandez, N., Hudec, M. R., Jackson, C. A.-L., Dooley, T. P., & Duffy, O. B. (2020). The competition for salt and kinematic interactions between minibasins during density-driven subsidence: Observations from numerical models. *Petroleum Geoscience*, *26*(1), 3–15. https://doi.org/10.1144/petgeo2019-051

Gabaix, X., Gopikrishnan, P., Plerou, V., & Stanley, H. E. (2003). A theory of power-law distributions in financial market fluctuations. *Nature*, *423*(6937), 267–270. https://doi.org/10.1038/nature01624

Galloway, W. E. (2008). Depositional evolution of the Gulf of Mexico sedimentary basin. *Sedimentary basins of the world*, *5*, 505–549.

Galloway, W. E., Ganey-Curry, P. E., Li, X., & Buffler, R. T. (2000). Cenozoic depositional history of the Gulf of Mexico basin. *AAPG Bulletin*, *84*(11), 1743–1774. https://doi.org/10.1306/8626c37f-173b-11d7-8645000102c1865d

Galy, V., France-Lanord, C., Beyssac, O., Faure, P., Kudrass, H., & Palhol, F. (2007). Efficient organic carbon burial in the Bengal fan sustained by the Himalayan erosional system. *Nature*, *450*(7168), 407–410. https://doi.org/10.1038/nature06273

Ganti, V., Straub, K. M., Foufoula-Georgiou, E., & Paola, C. (2011). Space-time dynamics of depositional systems: Experimental evidence and theoretical modeling of heavy-tailed statistics. *Journal of Geophysical Research*, *116*(F2), F02011. https://doi.org/10.1029/2010jf001893

Ge, Z., Gawthorpe, R. L., Zijerveld, L., & Oluboyo, A. (2019). Controls on variations in minibasin geometries: Lower Congo Basin, offshore Angola.

Gemmer, L., Ings, S. J., Medvedev, S., & Beaumont, C. (2004). Salt tectonics driven by differential sediment loading: Stability analysis and finite-element experiments. *Basin Research*, *16*(2), 199–218. https://doi.org/10.1111/j.1365-2117.2004.00229.x

Gilbert, G. (1877). *Report on the geology of the henry mountains*. Government Printing Office.

Hallet, B. (1990). Spatial self-organization in geomorphology: From periodic bedforms and patterned ground to scale-invariant topography. *Earth-Science Reviews*, *29*(1–4), 57–75. https://doi.org/10.1016/0012-8252(0)90028-t

Hudec, M. R., & Jackson, M. P. (2007). Terra infirma: Understanding salt tectonics. *Earth-Science Reviews*, *82*(1–2), 1–28. https://doi.org/10.1016/j.earscirev.2007.01.001

Hudec, M. R., Jackson, M. P., & Peel, F. J. (2013). Influence of deep Louann structure on the evolution of the northern Gulf of MexicoGulf of Mexico salt influence. *AAPG Bulletin*, *97*(10), 1711–1735. https://doi.org/10.1306/04011312074

Hudec, M. R., Jackson, M. P., & Schultz-Ela, D. D. (2009). The paradox of minibasin subsidence into salt: Clues to the evolution of crustal basins. *The Geological Society of America Bulletin*, *121*(1–2), 201–221. https://doi.org/10.1130/b26275.1

Hudec, M. R., Norton, I. O., Jackson, M. P., & Peel, F. J. (2013). Jurassic evolution of the Gulf of Mexico salt basin. *AAPG Bulletin*, *97*(10), 1683–1710. https://doi.org/10.1306/04011312073

Ings, S. J., & Beaumont, C. (2010). Shortening viscous pressure ridges, a solution to the enigma of initiating salt 'withdrawal' minibasins. *Geology*, *38*(4), 339–342. https://doi.org/10.1130/g30520.1

Jackson, M., & Seni, S. (1983). Geometry and evolution of salt structures in a marginal rift basin of the Gulf of Mexico, east Texas. *Geology*, *11*(3), 131–135. https://doi.org/10.1130/0091-7613(1983)11<131:gaeoss>2.0.co;2

Jerolmack, D. J., & Mohrig, D. (2005). A unified model for subaqueous bed form dynamics. *Water Resources Research*, *41*(12), W12421. https://doi.org/10.1029/2005wr004329

Jervey, M. T. (1988). Quantitative geological modeling of siliciclastic rock sequences and their seismic expression. In C. K. Wilgus, B. S. Hastings, C. G. S. C. Kendall, H. W. Posamentier, C. A. Ross, & J. C. Van Wagoner (Eds.), *Sea level changes — an integrated approach* (pp. 47–69). Special Publication. Society of Economic Paleontologists and Mineralogists (SEPM).

Jr Humphris, C. (1979). Salt movement on continental slope, northern Gulf of Mexico. *AAPG Bulletin*, *63*(5), 782–798. https://doi.org/10.1306/2f9182d4-16ce-11d7-8645000102c1865d

Kagan, Y. Y. (2010). Earthquake size distribution: Power-law with exponent β≡ 12? *Tectonophysics*, *490*(1–2), 103–114. https://doi.org/10.1016/j.tecto.2010.04.034

Kane, I. A., Clare, M. A., Miramontes, E., Wogelius, R., Rothwell, J. J., Garreau, P., & Pohl, F. (2020). Seafloor microplastic hotspots controlled by deep-sea circulation. *Science*, *368*(6495), 1140–1145. https://doi.org/10.1126/science.aba5899

Kilsdonk, B., Graham, R., & Pilcher, R. (2010). Deep water Gulf of Mexico sub-salt structural framework. In *Offshore technology conference*. OTC.20937.

Kolla, V., Bandyopadhyay, A., Gupta, P., Mukherjee, B., & Ramana, D. V. (2012). Morphology and internal structure of a recent upper Bengal fan-valley complex. *Application of the Principles of Seismic Geomorphology to Continental-Slope and Base-of-Slope Systems: Case Studies from Seafloor and Near-Seafloor Analogues*, 347–369. https://doi.org/10.2110/pec.12.99.0347

Kolmogorov, A. N., & Bharucha-Reid, A. T. (2018). *Foundations of the theory of probability* (Second English Edition). Courier Dover Publications.

Kramer, K. V., & Shedd, W. W. (2017). *A 1.4-billion-pixel map of the Gulf of Mexico seafloor* (Vol. 98). EOS.

Lamb, M. P., Hickson, T., Marr, J. G., Sheets, B., Paola, C., & Parker, G. (2004). Surging versus continuous turbidity currents: Flow dynamics and deposits in an experimental intraslope minibasin. *Journal of Sedimentary Research*, *74*(1), 148–155. https://doi.org/10.1306/062103740148

Lamb, M. P., Toniolo, H., & Parker, G. (2006). Trapping of sustained turbidity currents by intraslope minibasins. *Sedimentology*, *53*(1), 147–160. https://doi.org/10.1111/j.1365-3091.2005.00754.x

Le, P. V., & Kumar, P. (2014). Power law scaling of topographic depressions and their hydrologic connectivity. *Geophysical Research Letters*, *41*(5), 1553–1559. https://doi.org/10.1002/2013gl059114

Mackin, J. H. (1948). Concept of the graded river. *The Geological Society of America Bulletin*, *59*(5), 463–512. https://doi.org/10.1130/0016-7606(1948)59[463:cotgr]2.0.co;2

Mark, D. M. (1988). Network models in geomorphology. In *Modelling geomorphological systems* (pp. 73–97). John Wiley and Sons.

Marković, D., & Gros, C. (2014). Power laws and self-organized criticality in theory and nature. *Physics Reports*, *536*(2), 41–74. https://doi.org/10.1016/j.physrep.2013.11.002

Martinez, J. D. (1991). Salt domes. *American Scientist*, *79*(5), 420–431.

McElroy, B., & Mohrig, D. (2009). Nature of deformation of sandy bed forms. *Journal of Geophysical Research*, *114*(F3). https://doi.org/10.1029/2008jf001220

Milliman, J. D., & Syvitski, J. P. (1992). Geomorphic/tectonic control of sediment discharge to the ocean: The importance of small mountainous rivers. *The Journal of Geology*, *100*(5), 525–544. https://doi.org/10.1086/629606

Mohriak, W. U., Szatmari, P., & Anjos, S. (2012). Salt: Geology and tectonics of selected Brazilian basins in their global context. *Geological Society*, *363*(1), 131–158. https://doi.org/10.1144/sp363.7

Mohrig, D., & Buttles, J. (2007). Shallow channels constructed by deep turbidity currents. *Geology*, *35*(2), 155–158. https://doi.org/10.1130/g22716a.1

Mosher, D. C., Campbell, D., Gardner, J., Piper, D., Chaytor, J., & Rebesco, M. (2017). The role of deep-water sedimentary processes in shaping a continental margin: The northwest Atlantic. *Marine Geology*, *393*, 245–259. https://doi.org/10.1016/j.margeo.2017.08.018

Naden, P. (1987). Modelling gravel-bed topography from sediment transport. *Earth Surface Processes and Landforms*, *12*(4), 353–367. https://doi.org/10.1002/esp.3290120403

Nasr-Azadani, M., & Meiburg, E. (2014). Turbidity currents interacting with three-dimensional seafloor topography. *Journal of Fluid Mechanics*, *745*, 409–443. https://doi.org/10.1017/jfm.2014.47

Newman, M. E. (2005). Power laws, Pareto distributions and Zipf's law. *Contemporary Physics*, *46*(5), 323–351. https://doi.org/10.1080/00107510500052444

Patacci, M., Haughton, P. D., & Mccaffrey, W. D. (2015). Flow behavior of ponded turbidity currents. *Journal of Sedimentary Research*, *85*(8), 885–902. https://doi.org/10.2110/jsr.2015.59

Peel, F. J. (2014). How do salt withdrawal minibasins form? Insights from forward modelling, and implications for hydrocarbon migration. *Tectonophysics*, *630*, 222–235. https://doi.org/10.1016/j.tecto.2014.05.027

Pettinga, L., Jobe, Z., Shumaker, L., & Howes, N. (2018). Morphometric scaling relationships in submarine channel–lobe systems. *Geology*, *46*(9), 819–822. https://doi.org/10.1130/g45142.1

Pilcher, R. S., Kilsdonk, B., & Trude, J. (2011). Primary Basins and their boundaries in the deep-water northern Gulf of Mexico: Origin, trap types, and petroleum system implications. *AAPG Bulletin*, *95*(2), 219–240. https://doi.org/10.1306/06301010004

Pindell, J., & Dewey, J. F. (1982). Permo-Triassic reconstruction of Western Pangea and the evolution of the Gulf of Mexico/Caribbean region. *Tectonics*, *1*(2), 179–211. https://doi.org/10.1029/tc001i002p00179

Pinto, C. M., Lopes, A. M., & Machado, J. T. (2012). A review of power laws in real life phenomena. *Communications in Nonlinear Science and Numerical Simulation*, *17*(9), 3558–3578. https://doi.org/10.1016/j.cnsns.2012.01.013

Pirmez, C., & Imran, J. (2003). Reconstruction of turbidity currents in Amazon channel. *Marine and Petroleum Geology*, *20*(6–8), 823–849. https://doi.org/10.1016/j.marpetgeo.2003.03.005

Planchon, O., & Darboux, F. (2002). A fast, simple and versatile algorithm to fill the depressions of digital elevation models. *Catena*, *46*(2–3), 159–176. https://doi.org/10.1016/s0341-8162(01)00164-3

Prather, B. E. (2003). Controls on reservoir distribution, architecture and stratigraphic trapping in slope settings. *Marine and Petroleum Geology*, *20*(6–8), 529–545. https://doi.org/10.1016/j.marpetgeo.2003.03.009

Prather, B. E. (2020). Controls on reservoir distribution, architecture and stratigraphic trapping in slope settings. In *Regional geology and tectonics* (pp. 481–515). Elsevier.

Pratson, L., & Haxby, W. F. (1996). What is the slope of the U.S. continental slope? *Geology*, *24*(1), 3–6. https://doi.org/10.1130/0091-7613(1996)024<0003:witsot>2.3.co;2

Pratson, L. F., Nittrouer, C. A., Wiberg, P. L., Steckler, M. S., Swenson, J. B., Cacchione, D. A., et al. (2007). Seascape evolution on clastic continental shelves and slopes. In C. A. Nittrouer, J. A. Austin, M. E. Field, J. H. Kravitz, J. P. M. Syvitski, & P. L. Wiberg (Eds.), *Continental margin sedimentation: From sediment transport to sequence stratigraphy* (pp. 339–380). Blackwell Publishing Ltd.

Reece, J. K., Dorrell, R. M., & Straub, K. M. (2024). Circulation of hydraulically ponded turbidity currents and the filling of continental slope minibasins. *Nature Communications*, *15*(1), 2075. https://doi.org/10.1038/s41467-024-46120-2

Rowan, M. G. (2022). The ocean-continent transition of late synrift salt basins: Extension and evaporite deposition. In *The southern Gulf of Mexico and global analogs*.

Salvador, A. (1991). Origin and development of the Gulf of Mexico basin. In A. Salvador (Ed.), *The Gulf of Mexico basin, volume J: The geology of North America* (pp. 131–180). Geological Society of America.

Schultz-Ela, D. D., Jackson, M. P., & Vendeville, B. (1993). Mechanics of active salt diapirism. *Tectonophysics*, *228*(3–4), 275–312. https://doi.org/10.1016/0040-1951(93)90345-k

Simpson, G., & Schlunegger, F. (2003). Topographic evolution and morphology of surfaces evolving in response to coupled fluvial and hillslope sediment transport. *Journal of Geophysical Research*, *108*(B6). https://doi.org/10.1029/2002jb002162

Slowey, N., Bryant, W. R., Bean, D. A., Young, A. G., & Gartner, S. (2003). Sedimentation in the vicinity of the Sigsbee escarpment during the last 25,000 yrs. In *Offshore technology conference*. OTC.15159.

Smith, J. D., & McLean, S. R. (1977). Spatially averaged flow over a wavy surface. *Journal of Geophysical Research*, *82*(12), 1735–1746. https://doi.org/10.1029/jc082i012p01735

Smith, R. (2004). Silled sub-basins to connected tortous corridors: Sediment distribution systems on topographically complex sub-aqueous slopes. In S. A. Lomas & P. Josevh (Eds.), *Confined turbidite systems* (pp. 23–43). Geological Society.

Sornette, D. (2006). *Critical phenomena in natural sciences: Chaos, fractals, selforganization and disorder: Concepts and tools*. Springer Science and Business Media.

Soutter, E. L., Bell, D., Cumberpatch, Z. A., Ferguson, R. A., Spychala, Y. T., Kane, I. A., & Eggenhuisen, J. T. (2021). The influence of confining topography orientation on experimental turbidity currents and geological implications. *Frontiers in Earth Science*, *8*, 540633. https://doi.org/10.3389/feart.2020.540633

Steffens, G. S., Biegert, E. K., Sumner, H. S., & Bird, D. (2003). Quantitative bathymetric analyses of selected deepwater siliciclastic margins: Receiving basin configurations for deepwater fan systems. *Marine and Petroleum Geology*, *20*(6–8), 547–561. https://doi.org/10.1016/j.marpetgeo.2003.03.007

Stricker, S., Jones, S. J., Meadows, N., & Bowen, L. (2018). Reservoir quality of fluvial sandstone reservoirs in salt-walled mini-basins: An example from the seagull field, Central Graben, North Sea, UK. *Petroleum Science*, *15*(1), 1–27. https://doi.org/10.1007/s12182-017-0206-x

Talling, P. J., Baker, M. L., Pope, E. L., Ruffell, S. C., Jacinto, R. S., Heijnen, M. S., et al. (2022). Longest sediment flows yet measured show how major rivers connect efficiently to deep sea. *Nature Communications*, *13*(1), 1–15. https://doi.org/10.1038/s41467-022-31689-3

Talling, P. J., Hage, S., Baker, M. L., Bianchi, T. S., Hilton, R. G., & Maier, K. L. (2023). The global turbidity current pump and its implications for organic carbon cycling. *Annual Review of Marine Science*, *16*(1), 105–133. https://doi.org/10.1146/annurev-marine-032223-103626

Thorne, J., & Swift, D. (1992). Sedimentation on continental margins, II: Application of the regime concept. In *Shelf sand and sandstone bodies: Geometry, facies and sequence stratigraphy* (pp. 33–58).

van Andel, T. H., & Komar, P. D. (1969). Ponded sediments of the Mid-Atlantic Ridge between 22 and 23 north latitude. *The Geological Society of America Bulletin*, *80*(7), 1163–1190. https://doi.org/10.1130/0016-7606(1969)80[1163:psotmr]2.0.co;2

White, E. P., Enquist, B. J., & Green, J. L. (2008). On estimating the exponent of power-law frequency distributions. *Ecology*, *89*(4), 905–912. https://doi.org/10.1890/07-1288.1

Worrall, D., & Snelson, S. (1989). Evolution of the northern Gulf of Mexico, with emphasis on Cenozoic growth faulting and the role of salt. *The Geology of North America—An Overview*, 97–138. https://doi.org/10.1130/dnag-gna-a.97

Wu, Q. (2021). Lidar: A Python package for delineating nested surface depressions from digital elevation data. *Journal of Open Source Software*, *6*(59), 2965. https://doi.org/10.21105/joss.02965

Wu, Q., Lane, C. R., Wang, L., Vanderhoof, M. K., Christensen, J. R., & Liu, H. (2019). Efficient delineation of nested depression hierarchy in digital elevation models for hydrological analysis using level-set method. *JAWRA Journal of the American Water Resources Association*, *55*(2), 354–368. https://doi.org/10.1111/1752-1688.12689

Wu, S., Bally, A. W., & Cramez, C. (1990). Allochthonous salt, structure and stratigraphy of the North-Eastern Gulf of Mexico. Part II: Structure. *Marine and Petroleum Geology*, *7*(4), 334–370. https://doi.org/10.1016/0264-8172(90)90014-8

Xu, J. P., Nobel, M. A., & Rosenfeld, L. K. (2004). In-situ measurments of velocity structure within turbidity currents. *Geophysical Research Letters*, *31*(9). https://doi.org/10.1029/2004GL019718